


## Research Article

# Sedimentation rate changes across the Chinese Loess Plateau from luminescence dating of Malan loess in the Sanmen Gorge

Gang Hu<sup>a</sup> , Huiying Wang<sup>a</sup>, Bo Xu<sup>a</sup>, Ping Wang<sup>a</sup>, Liubing Xu<sup>b</sup>, Jinming Xie<sup>b</sup>, Xing Wang<sup>c</sup>, Long Qiao<sup>d</sup>, Changhui Guo<sup>d</sup>, Junkang Wang<sup>e</sup>, Jiafu Zhang<sup>e</sup>, Wenxu Wang<sup>f</sup>, La Ta<sup>d</sup> and Lei Wang<sup>d\*</sup>

<sup>a</sup>State Key Laboratory of Earthquake Dynamics, Institute of Geology, China Earthquake Administration, Beijing 100029, China; <sup>b</sup>Department of Geographical Sciences, South China Normal University, Guangzhou 510631, China; <sup>c</sup>Key Laboratory of Western China's Environmental Systems (Ministry of Education), College of Earth and Environmental Sciences, Lanzhou University, Lanzhou 730000, China; <sup>d</sup>First Monitoring and Application Center, China Earthquake Administration, Tianjin, 300180, China; <sup>e</sup>Key Laboratory for Earth Surface Processes, Department of Geography, Peking University, Beijing 100871, China and <sup>f</sup>Earthquake Administration of Henan Province, Zhengzhou 450016, China

## Abstract

The Chinese Loess Plateau (CLP), recognized as the world's largest loess plateau, has been a subject of ongoing debate regarding the continuity of its sedimentary loess sequence due to its intricate depositional environment. In this study, we conducted dating on a 9.8-m-long Malan loess core obtained from the Sanmen Gorge in the southern CLP using optically stimulated luminescence (OSL). The OSL dates indicate loess deposition between 52.4 and 11.3 ka, with no apparent hiatus on a millennial scale, and a sedimentation rate (SR) exhibiting six distinct episodes. Additionally, a comprehensive review of 613 OSL ages from 18 sections at 14 sites across the CLP was conducted. The results reveal loess deposition at most sites shows no apparent hiatus on a millennial scale over the past 60 ka, except for two specific locations. High SR episodes during Marine Isotope Stage (MIS) 3 across the CLP were attributed to heightened dust emissions from the source region and an enhanced dust deposition efficiency, while MIS 2 deposits were influenced by an intensified East Asian winter monsoon. Low SR episodes during MIS 1 at most sites were likely associated with reduced atmospheric transportation and pedogenesis. Spatially heterogeneous SR variations across the CLP might be influenced by local depositional environments.

**Keywords:** Chinese Loess Plateau, Sanmen Gorge, OSL dating, sedimentary rate change

(Received 8 February 2023; accepted 5 March 2024)

## INTRODUCTION

The Chinese Loess Plateau (CLP), situated in northern China and encompassing an area of approximately  $\sim 4.5 \times 10^5$  km<sup>2</sup>, stands as the world's largest loess plateau. Characterized by a mean thickness of  $\sim 100$  m (Xiong et al., 2014), the loess–paleosol sequences within the CLP offer the most extensive and detailed terrestrial records of paleoenvironmental changes (e.g., An et al., 1991a, 1991b; Lu et al., 1999; Ding et al., 2002; Sun, 2002; Maher, 2016). Establishing a reliable chronostratigraphic framework is fundamental to loess research. Initially, paleomagnetic dating was applied to sedimentary samples from the CLP, leading to the creation of a more accurate chronostratigraphic framework utilizing magnetic susceptibility, grain-size variation, and orbital tuning methods (Li et al., 1974; An et al., 1977; Kukla et al., 1988; Porter and An, 1995). The lack of suitable organic materials for <sup>14</sup>C dating has prompted widespread use of optically stimulated luminescence (OSL) for dating loess deposits in China (e.g., Li and Wintle, 1992; Lai and Wintle, 2006; Stevens et al.,

2006, 2008, 2013, 2016, 2018; Lai, 2010; Kang et al., 2011, 2013, 2015; Dong et al., 2015; Yi et al., 2015; Li et al., 2016, 2018; Perić et al., 2019; Constantin et al., 2021). Most OSL dates consistently indicate loess deposition shows no apparent hiatus on a millennial scale during the late Pleistocene. However, Stevens et al. (2018) contested this consensus, asserting the presence of significant hiatuses ( $\sim 55$  ka) over the last  $\sim 250$  ka within the loess sections at Jinbian (JB) on the northern CLP and challenging established interpretations of loess records. Conversely, OSL dates also reveal that sedimentation rates (SR) across the CLP were considerably higher during the last glacial maximum (LGM) compared with the last deglaciation (Kang et al., 2013, 2015). The CLP is bordered by the Badain Jaran and Tengger Deserts and the Yellow River (YR) to its northwest and north, respectively. To the west and south, the Qilian, eastern Kunlun, and Qinling Mountain ranges further shape its complex loess depositional environment, potentially contributing to diverse depositional characteristics at different locations (Fig. 1).

In this study, a 9.8 m core was extracted from Terrace 2 (T2) along the YR in the Sanmen Gorge (SMG) region. Utilizing the OSL method, we dated the loess sediment within the core and subsequently reconstructed the SR of the core based on these OSL dates. Through a comparative analysis of OSL ages derived from loess deposits at 14 sites, we conducted a comprehensive review

\*Corresponding author email address: hswang@fmac.ac.cn

**Cite this article:** Hu G et al (2024). Sedimentation rate changes across the Chinese Loess Plateau from luminescence dating of Malan loess in the Sanmen Gorge. *Quaternary Research* 1–16. <https://doi.org/10.1017/qua.2024.18>

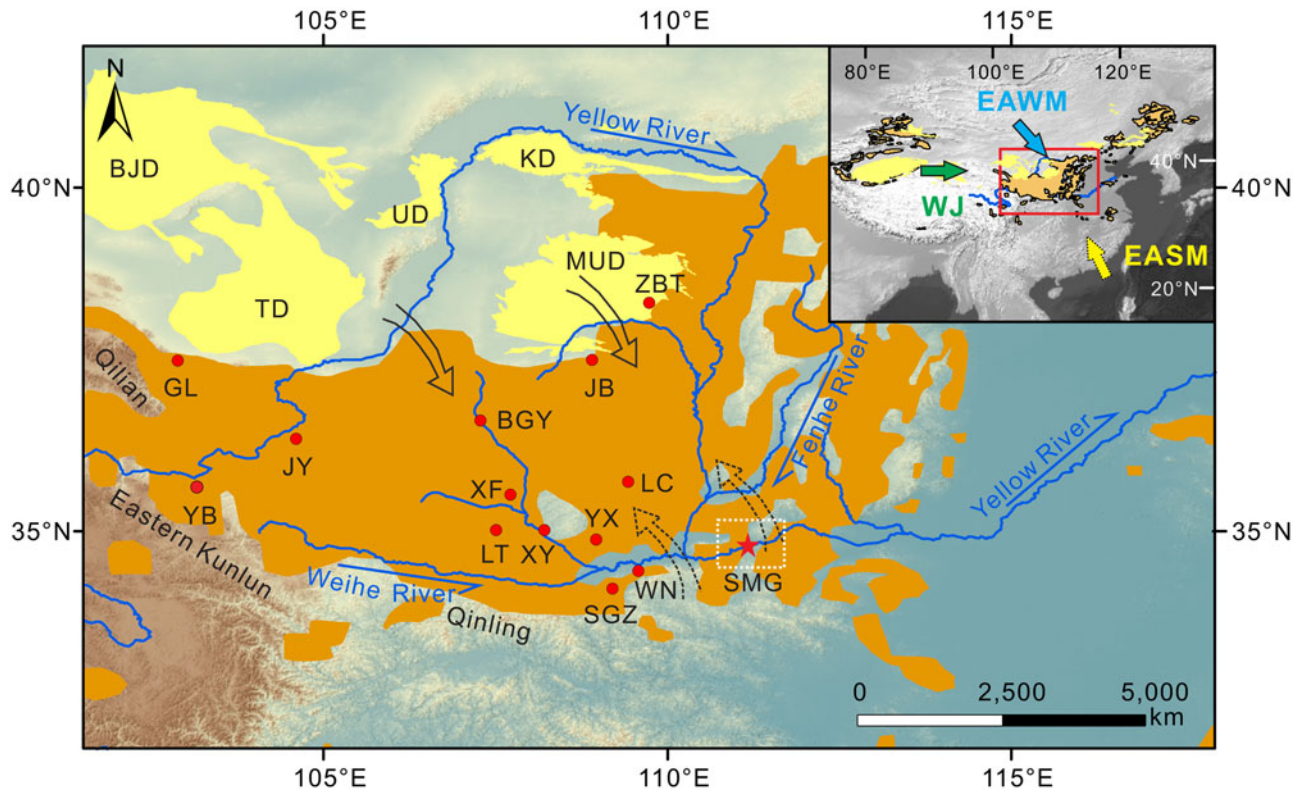


**Figure 1.** Digital elevation model image showing the locations of the loess, deserts, Yellow River (YR) and loess sites on the Chinese Loess Plateau (CLP) (modified according to Liu et al., 2020). BJD, Badain Jaran Desert; KD, Kubuqi Desert; MUD, Mu Us Desert; TD, Tengger Desert; UD, Ulan Buh Desert; WJ, westerly jet. The filled circles represent the loess sites; their full names and references are listed in Table 2. The solid, dashed, and dotted lines represent the East Asian winter monsoon (EAWM), East Asian summer monsoon (EASM), and the study area in Fig. 2 respectively.

of the variations in SRs across the CLP, engaging in discussions regarding the potential drivers behind these observed changes.

## GEOMORPHOLOGICAL SETTING AND STRATIGRAPHY

### Geomorphological setting

The SMG Basin is situated along the southeastern margins of the CLP, as illustrated in Figure 1. This basin constitutes the eastern segment of the broader Weihe Basin. Its geographic boundaries are defined by the Zhongtiao and Xiao Mountain ranges, which represent subranges of the eastern Qinling Mountains, marking the northern and southern perimeters of the SMG Basin, respectively. This confinement results in a width ranging from 20 to 30 km (Fig. 2a). The YR traverses the valley bottom from west to east. The maximum depth of the loess deposits in this basin is approximately ~150 m, comprising intact Pliocene red clay and Quaternary Lishi/Malan loess (Xiong et al., 2017, 2018; Li et al., 2017). The mean annual precipitation in the SMG Basin ranges between 500 and 800 mm, with a significant portion occurring during the summer months and contributing substantially to the annual precipitation total (Zhao et al., 2020).

In 2018, a 150-m-long core labeled SMX19 (34.80°, 111.17°, 351 m above sea level [m asl]) was drilled on T2 along the YR. The drilling location was situated ~450 m from the YR banks and around 35 m above the river's mean water level, as illustrated in Figure 2a. T2 was formed around ~129 ka, according to Hu et al. (2017). The core was extracted from a freshly excavated floor, prepared before constructing a house. The original ground level was approximately ~2 m higher, indicating that the final top of the

core was ~2 m deeper than the recorded depth. The core had a diameter of ~108 mm, with a mean coring recovery rate of 95%.

### Stratigraphy and sampling

The sediment in the lower section, from 9.8 to 108.7 m of the core, is characterized by pale yellow silty sand-clay exhibiting weak horizontal bedding (Supplementary Fig. S1). This composition strongly suggests that it represents YR fluvial sediment, as detailed in Wang et al. (2022). In contrast, the upper 9.8 m of the core is composed of pale yellow sandy silt, containing a few snail shells (Fig. 2b–d). Notably, this layer aligns with the Malan loess, as evidenced by the excavation of hundreds of Western Han Dynasty (206 BCE–24 CE) tombs on a nearby hill, approximately 200 m from the core (Shangguan, 2021). The loess covering these tombs measures around ~1–2 m in thickness, indicating an SR of approximately ~100 cm/ka during the Late Holocene.

The loess within the depth range of 2.5–9.8 m remained largely intact upon extraction from the liner tubes, as depicted in Figure 2b. Subsequently, immediate steps were taken to extract 4-cm-thick samples (SMX19-6 to SMX19-19) for OSL dating. These samples were carefully covered with aluminum foil to prevent exposure to sunlight. It is worth noting that the top 2.5 m of the core exhibited a loose structure, easily splintering after extraction from the liner tubes, which could potentially expose the sediments to sunlight. To mitigate this, a 2.2-m-deep pit was excavated adjacent to core SMX19, and five OSL samples (SMX19-1 to SMX19-5) were collected using

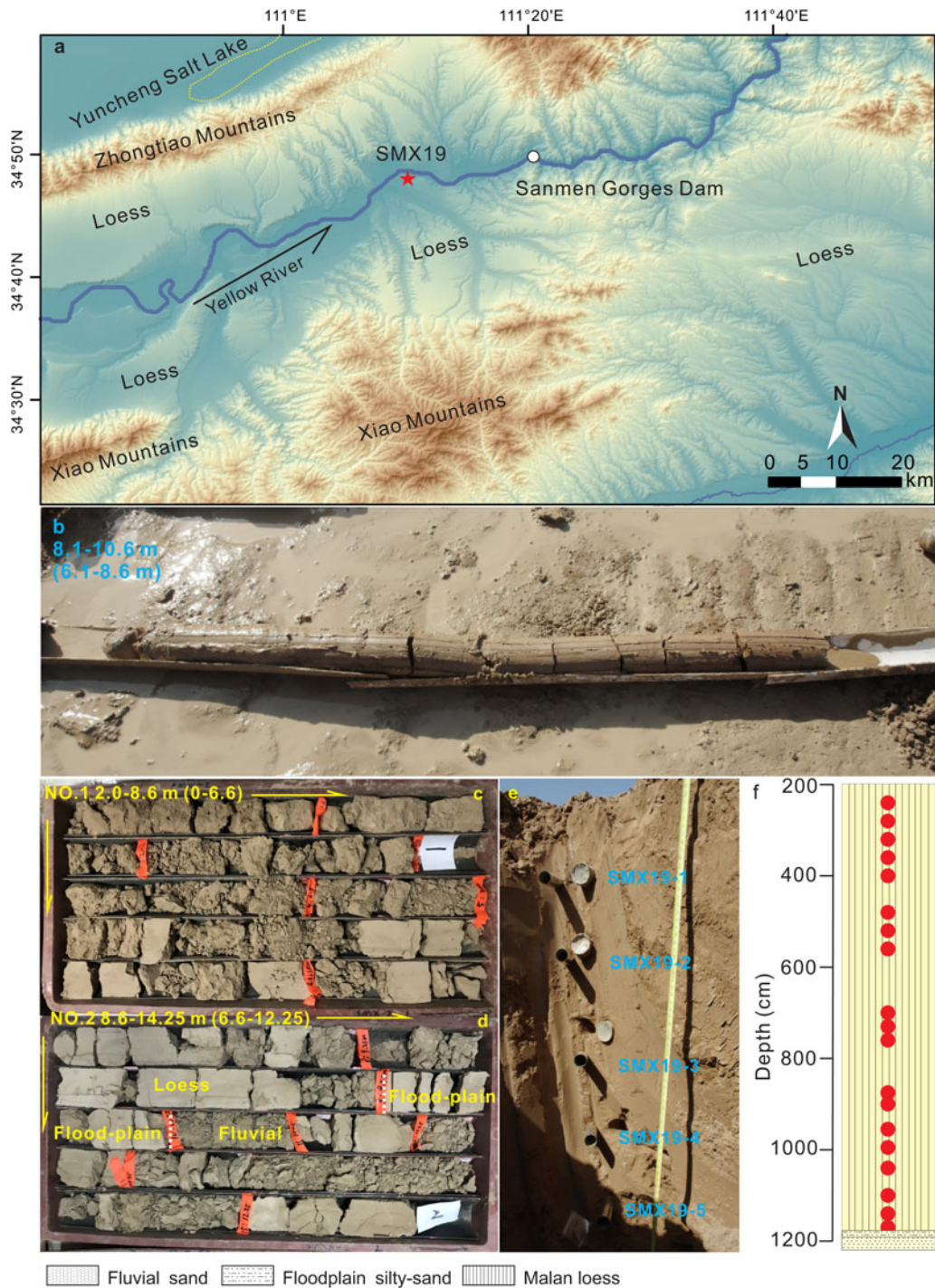


**Figure 2.** (a) Digital elevation model image showing the location of core SMX19. (b) Photograph showing a typical core extracted from a depth of 8.1–10.6 m (6.1–8.6 m). The core was drilled from a fresh floor dug during house construction; the original ground surface was ~2 m higher. The final top of the core was therefore corrected by ~2 m. (c and d) Photographs showing sedimentary properties of the extracted cores. (e) Photograph showing the sedimentary properties of the pit used for optically stimulated luminescence (OSL) sampling. (f) The sedimentary strata of core SMX19 and OSL samples.

stainless steel tubes (Fig. 2e). In total, 19 OSL samples were collected (Fig. 2f, Table 1). The remaining core underwent splitting in the laboratory to facilitate the analysis of its sedimentary characteristics, as shown in Figure 2c and d. A comprehensive sampling strategy was employed, resulting in the collection of 37 samples from the loess layers, 12 samples from the underlying floodplain–fluvial sediment (~10.0–12.0 m), and 2 samples

from the modern YR floodplain. These samples were specifically collected for grain-size analysis with the aim of exploring the provenance of the loess.

To further investigate the mechanisms behind SR changes over the past 60 ka across the CLP, we conducted a comprehensive review of high-resolution OSL sampling in loess sections across the CLP. This involved collating a substantial data set comprising

**Table 1.** Optically stimulated luminescence (OSL) dating results for loess samples extracted from the Sanmen Gorge region.<sup>a</sup>

Sample no.	Depth <sup>b</sup> (m)	U (ppm)	Th (ppm)	K (%)	WC <sup>c</sup> (%)	Dose rate (Gy/ka)		FGQ $D_e$ (Gy)	Polymineral MET-pIRIR $D_e$ (Gy)					FGQ age (ka)	Polymineral MET-pIRIR age (ka)				
						FGQ	Polymineral		50°C	100°C	150°C	200°C	250°C		50°C	100°C	150°C	200°C	250°C
SMX19-1	2.4 (0.4)	3.23 ± 0.16	13.90 ± 0.70	1.77 ± 0.09	15 ± 3 (15.6)	3.80 ± 0.22	N/A	42.9 ± 0.9	N/A	N/A	N/A	N/A	N/A	11.3 ± 0.7	N/A	N/A	N/A	N/A	N/A
SMX19-2	2.8 (0.8)	3.03 ± 0.15	15.60 ± 0.78	1.80 ± 0.09	15 ± 3 (13.8)	3.90 ± 0.23	N/A	44.5 ± 0.5	N/A	N/A	N/A	N/A	N/A	11.4 ± 0.7	N/A	N/A	N/A	N/A	N/A
SMX19-3	3.2 (1.2)	3.08 ± 0.15	14.70 ± 0.74	1.79 ± 0.09	15 ± 3 (13.4)	3.83 ± 0.22	N/A	45.8 ± 0.9	N/A	N/A	N/A	N/A	N/A	12.0 ± 0.7	N/A	N/A	N/A	N/A	N/A
SMX19-4	3.6 (1.6)	2.97 ± 0.15	15.70 ± 0.79	1.79 ± 0.09	15 ± 3 (12.8)	3.87 ± 0.23	N/A	49.2 ± 0.8	N/A	N/A	N/A	N/A	N/A	12.7 ± 0.8	N/A	N/A	N/A	N/A	N/A
SMX19-5	4.0 (2.0)	3.14 ± 0.16	16.10 ± 0.81	1.79 ± 0.09	15 ± 3 (13.2)	3.95 ± 0.23	N/A	51.7 ± 0.6	N/A	N/A	N/A	N/A	N/A	13.1 ± 0.8	N/A	N/A	N/A	N/A	N/A
SMX19-6	4.8 (2.8)	2.95 ± 0.15	14.60 ± 0.73	1.65 ± 0.08	15 ± 3 (19.9)	3.63 ± 0.21	N/A	54.5 ± 0.6	N/A	N/A	N/A	N/A	N/A	15.0 ± 0.9	N/A	N/A	N/A	N/A	N/A
SMX19-7	5.2 (3.2)	2.81 ± 0.14	14.00 ± 0.70	1.65 ± 0.08	15 ± 3 (17.4)	3.54 ± 0.21	N/A	70.5 ± 0.6	N/A	N/A	N/A	N/A	N/A	19.9 ± 1.2	N/A	N/A	N/A	N/A	N/A
SMX19-8	5.6 (3.6)	2.82 ± 0.14	13.70 ± 0.69	1.70 ± 0.09	15 ± 3 (21.3)	3.55 ± 0.21	N/A	75.7 ± 0.7	N/A	N/A	N/A	N/A	N/A	21.3 ± 1.2	N/A	N/A	N/A	N/A	N/A
SMX19-9	7.0 (5.0)	3.01 ± 0.15	14.80 ± 0.74	1.76 ± 0.09	15 ± 3 (18.1)	3.74 ± 0.22	N/A	84.6 ± 1.3	N/A	N/A	N/A	N/A	N/A	22.6 ± 1.4	N/A	N/A	N/A	N/A	N/A
SMX19-10	7.3 (5.3)	3.05 ± 0.15	15.30 ± 0.77	1.77 ± 0.09	15 ± 3 (17.9)	3.80 ± 0.22	N/A	99.1 ± 1.0	N/A	N/A	N/A	N/A	N/A	26.0 ± 1.6	N/A	N/A	N/A	N/A	N/A
SMX19-11	7.6 (5.6)	3.17 ± 0.16	15.60 ± 0.78	1.78 ± 0.09	15 ± 3 (16.3)	3.87 ± 0.23	N/A	112.5 ± 2.4	N/A	N/A	N/A	N/A	N/A	29.1 ± 1.8	N/A	N/A	N/A	N/A	N/A
SMX19-12	8.75 (6.75)	3.35 ± 0.17	16.00 ± 0.80	1.74 ± 0.09	15 ± 3 (20.8)	3.91 ± 0.24	N/A	137.0 ± 3.2	N/A	N/A	N/A	N/A	N/A	35.0 ± 2.3	N/A	N/A	N/A	N/A	N/A
SMX19-13	9.0 (7.0)	3.54 ± 0.18	15.80 ± 0.79	1.76 ± 0.09	15 ± 3 (20.0)	3.97 ± 0.24	N/A	164.8 ± 1.1	N/A	N/A	N/A	N/A	N/A	41.5 ± 2.5	N/A	N/A	N/A	N/A	N/A
SMX19-14	9.55 (7.55)	3.44 ± 0.17	16.30 ± 0.82	1.77 ± 0.09	15 ± 3 (14.0)	3.99 ± 0.24	N/A	166.4 ± 2.5	N/A	N/A	N/A	N/A	N/A	41.7 ± 2.6	N/A	N/A	N/A	N/A	N/A
SMX19-15	9.95 (7.95)	3.66 ± 0.18	16.20 ± 0.81	1.78 ± 0.09	15 ± 3 (16.3)	4.05 ± 0.25	N/A	168.4 ± 3.8	N/A	N/A	N/A	N/A	N/A	41.6 ± 2.7	N/A	N/A	N/A	N/A	N/A
SMX19-16	10.4 (8.4)	3.94 ± 0.20	15.10 ± 0.76	1.68 ± 0.08	15 ± 3 (24.9)	3.95 ± 0.24	4.72 ± 0.25	171.9 ± 6.8	135.0 ± 3.1	160.6 ± 10.1	178.1 ± 8.7	197.0 ± 10.9	191.0 ± 12.7	43.5 ± 3.2	28.6 ± 1.7	34.0 ± 2.8	37.7 ± 2.7	41.7 ± 3.2	40.5 ± 3.5
SMX19-17	11.0 (9.0)	3.63 ± 0.18	14.80 ± 0.74	1.67 ± 0.08	15 ± 3 (22.1)	3.82 ± 0.23	4.56 ± 0.24	160.0 ± 8.5	126.8 ± 2.2	163.6 ± 8.2	186.2 ± 9.0	194.0 ± 11.7	206.1 ± 3.9	41.8 ± 3.4	27.8 ± 1.6	35.9 ± 2.6	40.9 ± 2.9	42.6 ± 3.4	45.3 ± 2.6
SMX19-18	11.4 (9.4)	3.27 ± 0.16	14.60 ± 0.73	1.66 ± 0.08	15 ± 3 (20.8)	3.69 ± 0.22	N/A	174.0 ± 2.4	N/A	N/A	N/A	N/A	N/A	47.2 ± 2.9	N/A	N/A	N/A	N/A	N/A
SMX19-19	11.7 (9.7)	2.49 ± 0.12	11.20 ± 0.56	1.68 ± 0.08	15 ± 3 (18.9)	3.19 ± 0.18	3.72 ± 0.18	167.5 ± 3.9	120.2 ± 1.9	148.1 ± 4.4	173.6 ± 3.5	194.9 ± 4.0	207.0 ± 3.2	52.4 ± 3.1	32.3 ± 1.7	39.8 ± 2.3	46.6 ± 2.5	52.4 ± 2.8	55.6 ± 2.9

<sup>a</sup>Abbreviations:  $D_e$ , equivalent dose; FGQ, fine-grained quartz; IR, infrared; IRSL, infrared stimulated luminescence; MET-pIRIR, multi-elevated temperature post-IR IRSL protocol; WC, water content<sup>b</sup>Values and values in brackets are the burial depth and drilling depth for the OSL samples, respectively.<sup>c</sup>WC was assumed to be 15 ± 3%. Values in brackets are the laboratory-measured WC.

**Table 2.** Details of the sections of the Chinese Loess Plateau (CLP) dated using the optically stimulated luminescence (OSL) dating method.

Sites <sup>a</sup>	Location <sup>b</sup>	Depth (m)	Material	Numbers of 60–0 ka dates <sup>c</sup>	Mean SR <sup>d</sup>		References
					High SR episodes	Low SR episodes	
Gulang (GL)	37.49°N, 102.88°E, 2400 m	20.0	Quartz (Q)	20	44.9 (56.2–55.0) 46.4 (52.4–34.9) 53.0 (24.8–13.2)	38.0 (55.0–52.4) 34.9 (34.9–24.8)	Sun et al., 2012
Jingyuan (JY E1)	36.35°N, 104.60°E, 2110 m	24.0	Quartz (Q)	27	70.0 (28.1–13.4) 108.8 (0.8–0.1)	45.1 (60.0–28.1) 3.9 (13.4–0.8)	Sun et al., 2010
Jingyuan (JY E2)		20.0	Quartz (Q)	25	68.8 (33.5–12.5)	44.1 (45.7–33.5) 9.7 (12.5–1.8)	Sun et al., 2012
Zhenbeitai (ZBT)	38.3283°N, 109.7309°E, 1187 m	4.75	Quartz (Q), K-feldspar (F)	24 (12Q, 12F)	36.7 (15.8–11.3) 50.2 (7.0–2.5)	11.4 (11.3–7.0)	Wu et al., 2019
Jingbian (JB)	37.4996°N, 108.9008°E, 1715 m	4.95	Quartz (Q), K-feldspar (F)	110 (55Q, 55F)	60.4 (18.6–13.6)	5.1 (60.0–56.0) 18.6 (13.6–2.4)	Stevens et al., 2018
Yuanbao (YB)	35.6460°N, 103.1513°E, 2040 m	20.72	Quartz (Q)	30	79.3 (27.8–13.4)	43.9 (46.0–27.8) 12.6 (13.4–0.4)	Rao et al., 2013
Beiguoyuan (BGY E1)	36.6184°N, 107.2826°E, 1545 m	2.85	Quartz (Q)	21	83.8 (5.1–0.1)	12.9 (15.5–5.1)	Stevens et al., 2006, 2008
Beiguoyuan (BGY E2)		12.6	Quartz (Q)	79	140.9 (24.8–18.1)	39.9 (37.5–24.8) 10.3 (18.1–7.7)	Stevens et al., 2006, 2008
Xifeng (XF E1)	35.5359°N, 107.7204°E, 1281 m	4.3	Quartz (Q)	40	16.2 (41.8–22.0) 212.9 (1.6–0.9)	7.9 (60.0–41.8) 2.4 (22.0–1.6)	Stevens et al., 2016
Xifeng (XF E2)		5.1	Quartz (Q)	45	26.1 (16.5–14.5)	11.9 (31.6–16.5) 14.0 (14.5–0.1)	Stevens et al., 2006
Lingtai (LT)	35.0208°N, 107.5092°E, 1290 m	5.6	Quartz (Q)	43	37.1 (43.9–38.1) 33.1 (16.7–15.2)	11.9 (38.1–16.7) 3.7 (15.2–1.9)	Perić et al., 2019
Xunyi (XY)	35.0236°N, 108.2059°E, 1151 m	6.7	Quartz (Q)	30	18.2 (46.8–33.8) 23.7 (26.6–22.3) 17.2 (9.8–3.6)	6.8 (33.8–26.6) 8.0 (22.3–9.8)	Stevens et al., 2008
Luochuan (LC E1)	35.7500°N, 109.4166°E, 1050 m	7.5	Quartz (Q)	19	19.8 (60.0–49.6) 15.7 (40.8–24.0) 26.9 (12.8–10.8) 47.3 (1.6–0.4)	11.7 (49.6–40.8) 4.4 (24.0–12.8) 5.4 (10.8–1.6)	Lu et al., 2007
Luochuan (LC E2)	35.7272°N, 109.4302°E, 1090 m	6.9	Quartz (Q)	8	N/A	14.0 (56.3–24.1)	Lai, 2010
Yaodian (YX)	34.8833°N, 108.9666°E, 690 m	3.7	Quartz (Q)	15	11.7 (44.0–30.3)	7.2 (30.3–1.5)	Dong et al., 2015
Shiguanzi (SGZ)	34.1728°N, 109.1960°E, 708 m	2.0	Quartz (Q)	18	9.8 (30.6–29.7) 8.9 (25.6–21.1) 282.7 (0.6–0.1)	4.8 (29.7–25.6) 4.5 (21.1–0.6)	Stevens et al., 2006
Weinan (WN)	34.4275°N, 109.5771°E, 660 m	6.4	Quartz (Q)	40	21.7 (49.4–43.7) 16.7 (23.0–21.8) 51.0 (10.1–9.3) 497.2 (0.74–0.69)	12.3 (59.5–49.4) 14.0 (43.7–23.0) 8.4 (21.8–10.1) 4.7 (9.3–0.74)	Kang et al., 2013
Sanmen Gorge (SMG)	34.80°N, 111.17°E, 351 m	9.7	Quartz (Q)	19	26.0 (47.4–39.7) 31.9 (26.2–19.8) 49.9 (16.1–10.7)	18.1 (50.7–47.4) 14.9 (39.7–26.2) 13.7 (19.8–16.1)	This study

<sup>a</sup>Letters in parentheses are abbreviations for the sites used in this study.

<sup>b</sup>m asl, meters above sea level.

<sup>c</sup>Values in parentheses are OSL age numbers dated using quartz (Q) and K-feldspar (F), respectively.

<sup>d</sup>Sedimentation rate (SR; in cm/ka) with values in parentheses showing the intervals of high and low SR episodes (in ka).

a total of 613 OSL ages derived from 18 sections at 14 different sites on the CLP, as outlined in Table 2. Figure 1 illustrates the geographic distribution of these sites, with six located on the

northern and northwestern CLP (ZBT, JB, BGY, JY, YB, and GL), five on the central CLP (XF, LT, XY, YX, and LC), and three on the southern CLP (SGZ, WN, and SMG).

## METHODOLOGY

### Grain-size analysis

Sample pretreatment for grain-size analysis adhered to the methodology established by Sun et al. (2002). The sediment was first treated with 30% H<sub>2</sub>O<sub>2</sub> to remove any organic material and 10% HCl to remove any carbonates (Konert and Vandenberghe, 1997). The samples were then deflocculated using a 0.05 M solution of (NaPO<sub>3</sub>)<sub>6</sub>, before finally being measured using a Malvern Mastersizer 3000 laser grain-size analyzer. Water was used as the dispersant, with a refractive index (RI) = 1.33 at 20°C. When calculating particle-size distributions with Mie theory, the default refractive (1.56) and absorption (0.01) indices were applied. Three replicate analyses indicated an analytical error of <2% for the mean grain size.

### OSL dating

Sample preparation was performed in a darkroom under a dimmed red light at the Institute of Geology, China Earthquake Administration. The unexposed sediment in the sample bags was treated with 10% HCl and 30% H<sub>2</sub>O<sub>2</sub> to remove carbonates and organic matter, respectively. Due to the limited sample amount of the core, only fine-grained (FG) fractions (4–11 μm) for all samples were isolated in our laboratory using our standard procedure (Zhang and Zhou, 2007). To isolate pure quartz, the FG quartz fractions were treated with 30% H<sub>2</sub>SiF<sub>6</sub> solution for several days (dependent on the intensity of infrared stimulated luminescence [IRSL] signals after etching). The purity of the quartz fractions was checked using infrared (IR) laser-diode stimulation (Duller, 2003). No detectable natural or regenerated (~10 Gy) IRSL signals were observed, suggesting that there were no feldspar contaminants present. The FG quartz and polymineral fractions were allowed to settle on 9.7 mm aluminum disks.

All OSL luminescence measurements were conducted using a Risø TL/OSL DA-20 luminescence reader. Blue (470 ± 30 nm) and IR (870 ± 40 nm) diodes were used for IR and blue-light stimulations. The OSL and IRSL signals were detected through U-340 filters and a filter pack of Schott BG-39 and Corning 7-59 filters, respectively. The single-aliquot regenerative-dose (SAR) and multi-elevated temperature post-IR IRSL protocol (MET-pIRIR) protocols were applied to measure the equivalent doses ( $D_e$ ) for FG quartz and polymineral samples, respectively (Murray and Wintle, 2000; Li and Li, 2011). Preheat and cut-heat temperature pairs of 220°C/160°C and 260°C/220°C were chosen for FG quartz samples SMX19-1 to SMX19-10 and SMX19-11 to SMX19-19, respectively, based on the dose-recovery test results (see “Luminescence Properties”). A five-step MET-pIRIR measurement procedure was followed, using a preheat temperature of 300°C for 10 s, with IR simulation temperature increasing from 50°C to 250°C at 50°C intervals (i.e., five temperatures of 50, 100, 150, 200 and 250°C) (Li and Li, 2011). The single-aliquot FG quartz stimulation time was 40 s; the first 0.64 s of the initial OSL signal, minus a background signal estimated from the integral of the last 3.2 s, was used for  $D_e$  calculations, with a 5 s initial OSL signal minus a 10 s background signal employed for FG polymineral samples (Fu et al., 2012).

The U and Th contents of all samples were measured using inductively coupled plasma mass-spectrometry. The K content was measured using flame photometry. Relative uncertainties for these elements were taken to be 5%. As listed in Table 1, the measured water contents (WC) were 12.8–24.9% for the loess samples. Assuming that the WC might change during burial time, WC values were taken to be 15 ± 3% for all samples. The dose rate of each

sample was calculated using the DR calculator program developed by Tsakalos et al. (2015); the results are listed in Table 1.

### SR calculation

The age–depth model for the SMG loess section was established using the Bacon model (Blaauw and Christen, 2011). The computations were executed with specified model parameters as follows: acc.shape = 1.5, acc.mean = 100–150 yr/cm, mem.mean = 0.7, and mem.strength = 4 (Stevens et al., 2018; Zhang et al., 2022). The model thickness was set at 10 cm, and the SRs of the core were determined using a mean value of 10 cm, in accordance with the recommendation of Li et al. (2018). The SRs of an additional 17 loess sections from 13 sites were also calculated using a similar method (Fig. 1). It is essential to note that Bayesian approaches considered the stratigraphic positions of the ages, contributing to a reduction in the error of the age–depth model (Blaauw and Christen, 2011). Consequently, errors in SRs were typically disregarded in the literature (Sun et al., 2012; Li et al., 2016, 2018; Stevens et al., 2018; Zhang et al., 2022).

## RESULTS

### Grain-size distribution

The grain-size distributions of the samples are presented in Figure 3, where the distributions have been categorized into four groups based on their sedimentary properties—loess, paleo-floodplain, paleofluvial, and modern floodplain sediments. Among the 10 fluvial samples, a predominant peak emerged at around ~105 μm, accompanied by a broad tail extending within the 0.3–30 μm range. One modern YR floodplain sample and the 37 loess samples exhibited similar particle-size distribution patterns. These patterns were characterized by asymmetric and positively skewed distributions, with primary peaks at ~50–90 μm and ~35–50 μm for the floodplain and loess sediments, respectively. Notably, the loess samples also displayed a subtle peak at ~450 μm, suggesting the presence of some coarse sand within them.

### Luminescence properties

As depicted in Figure 4a and b, the natural OSL signals of the FG quartz fractions for samples SMX19-7 and SMX19-18 exhibited

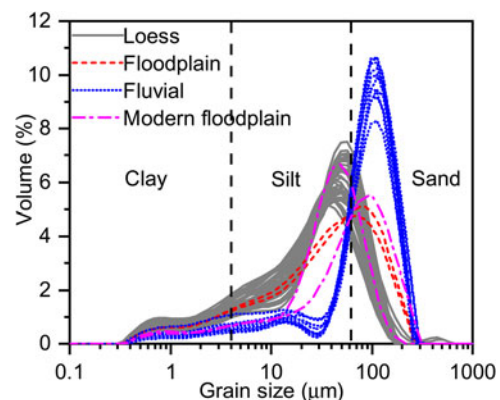


**Figure 3.** The particle-size distributions of loess and fluvial sand samples from core SMX19 and two modern floodplain samples from the Yellow River (YR).

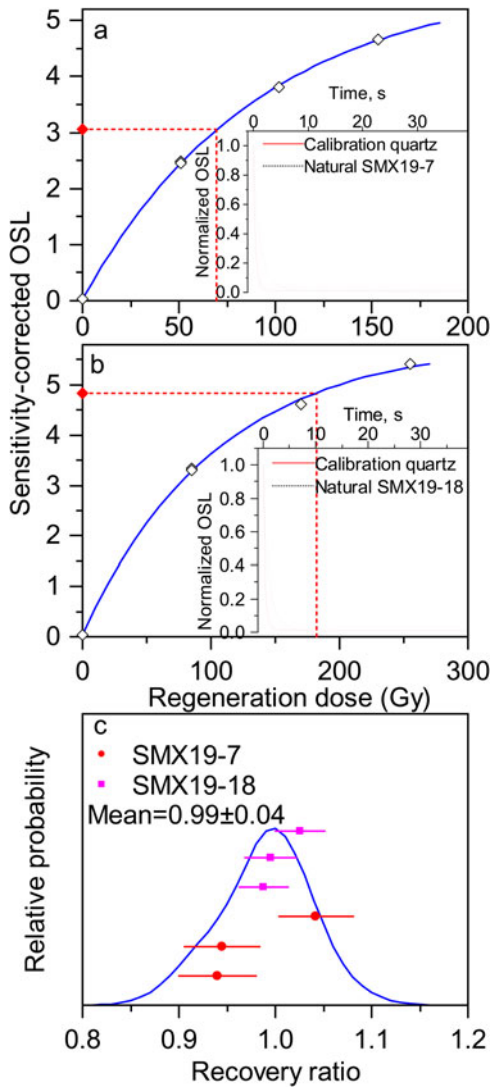


**Figure 4.** (a and b) Growth curves for samples SMX19-7 and SMX19-18 obtained using the single-aliquot regenerative-dose (SAR) protocol. The inserts show natural optically stimulated luminescence (OSL) decay curves of the same aliquots, for an aliquot of standard calibration quartz from the Risø National Laboratory. (c) Probability density function plots of the dose-recovery ratios for samples SMX19-7 and SMX19-18.

decay trends that closely resembled those of the Risø calibration quartz. The OSL signal experienced a rapid decay, dropping to approximately 10% of its original level within the initial stimulation period of around 3.0 s, indicating dominance by fast components in the OSL signals. Moreover, recuperation and recovery ratios from the growth curves indicated appropriate correction for any changes in sensitivity and negligible thermal transfers. The  $D_0$  values for samples SMX19-7 and SMX19-18 were ~92 and 105 Gy, respectively. The mean  $D_e$  value for our samples fell within the range of ~43–174 Gy (Table 1), representing 17–83% below the saturation intensity ( $2D_0$ ). These luminescence properties affirm the suitability of our FG quartz samples for OSL dating (Murray and Wintle, 2003; Wintle and Murray, 2006). To further assess the suitability of the SAR protocol for analyzing our samples, we conducted a dose-recovery test on two representative samples (SMX19-7 and SMX19-18). Considering the  $D_e$  values for these samples, preheat and cut-heat temperature pairs of 220°C/160°C and 260°C/220°C were applied to

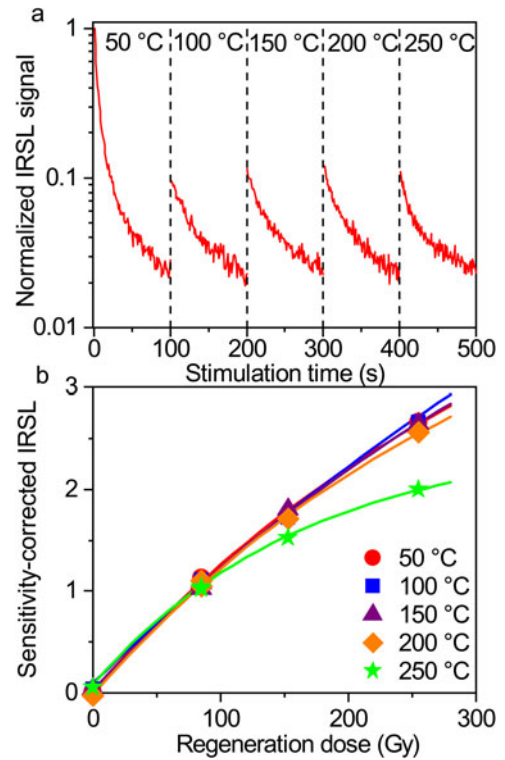


**Figure 5.** (a) Natural multi-elevated temperature post-infrared IR stimulated luminescence protocol (MET-pIRIR) decay curves for fine-grained (FG) polymineral fraction of sample SMX19-17, obtained at different stimulation temperatures. All data are normalized to the first point of the 50°C signal. (b) Growth curves for the MET-pIRIR signals of the same sample.

samples SMX19-7 and SMX19-18, respectively (Stevens et al., 2007). Each sample underwent measurement on three disks. The mean recovery ratios were found to be  $0.99 \pm 0.04$ , indicating that the preheat temperature was suitable for our quartz samples (Fig. 4c).

The natural IRSL signals of the FG polymineral fraction for sample SMX19-17, obtained at various stimulation temperatures, are illustrated in Figure 5a. Notably, the 50°C IRSL signal exhibited the highest intensity, while the IRSL intensities at other stimulation temperatures (100–250°C) were approximately comparable. This consistency aligns with the luminescence properties observed for the FG polymineral fraction from the Luochuan loess sequence (Fu et al., 2012). Furthermore, Figure 5b presents the growth curves derived from different MET-pIRIR signals of the same sample. The growth curves for stimulation temperatures ranging from 50 to 200°C demonstrated a general consistency, with the 250°C signal displaying smaller  $D_0$  values. This observed tendency mirrors that reported for coarse-grained K-feldspar (Li and Li, 2011) and FG polymineral fraction (Fu et al., 2012).

**DISCUSSION**

**Anomalous fading and comparison of the quartz and polymineral fractions**

To evaluate the anomalous fading of FG polymineral MET-pIRIR signals at various stimulation temperatures (i.e., 50–250°C), the  $D_e$  values of each aliquot were normalized to a MET-pIRIR stimulation temperature of 250°C. The  $D_e$  distributions for three

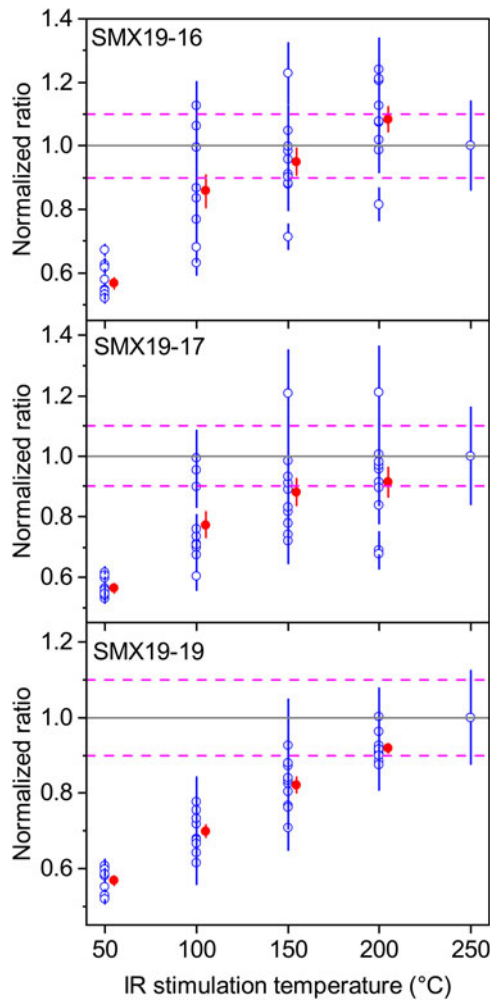


**Figure 6.** The normalized equivalent dose ( $D_e$ ) values for fine-grained (FG) polymineral samples determined using the multi-elevated temperature post-infrared IR stimulated luminescence protocol (MET-pIRIR) protocol. All data are normalized to the  $D_e$  values of the 250°C signal.

polymineral samples are presented in Figure 6 and Supplementary Figure S2. The normalized  $D_e$  values exhibited a linear increase from  $\sim 0.5$  to  $\sim 0.8$ – $0.9$  within the stimulation temperature range of 50–150°C. Subsequently, they plateaued at approximately 1.0 within a 10% error margin in the 200–250°C temperature range. This observation indicates the attainment of non-fading signals within the 200–250°C temperature range (Li and Li, 2011).

The comparison of FG quartz OSL ages and polymineral MET-pIRIR<sub>250</sub> ages for three samples (SMX19-16, SMX19-17, and SMX19-19) is illustrated in Figure 7. The two values exhibited consistency within a 10% error margin, further indicating that quartz ages were not underestimated due to the “saturation” effect. Consequently, FG quartz ages can be reliably employed to establish the chronology of our core. The subsequent discussion is based on the FG quartz OSL ages. A total of 19 loess samples were collected for OSL dating, with quartz OSL ages ranging from 11.3 ka (sample SMX19-1, depth 2.4 m) to 52.4 ka (sample SMX19-19, depth 11.7 m), as detailed in Table 1 and depicted in Figure 8.

#### Provenance of the loess in the SMG region

As shown in Figure 3, apart from the primary peaks at  $\sim 105$  and  $\sim 50$ – $90$   $\mu\text{m}$  for paleofluvial and modern floodplain sediments,

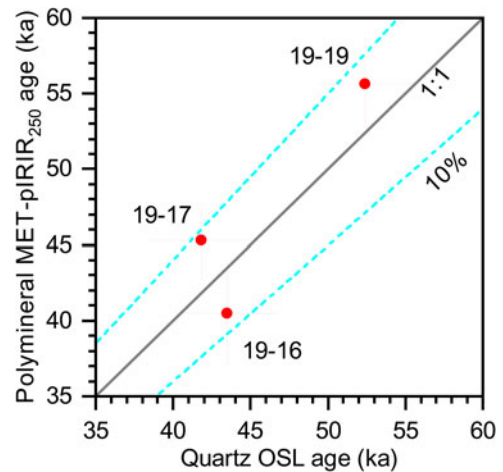


**Figure 7.** Comparison of fine-grained (FG) quartz optically stimulated luminescence (OSL) ages and polymineral multi-elevated temperature post-infrared IR stimulated luminescence protocol (MET-pIRIR<sub>250</sub>) ages. The dashed lines represent the  $\pm 10\%$  standard deviation errors from the 1:1 gray solid line.

the samples exhibit wide tails within a 0.3–30  $\mu\text{m}$  range. These clay and silt components represent loess sediments transported by the YR (Wang *et al.*, 2016). Conversely, the primary peak for the loess sediment within our core falls between  $\sim 35$  and 50  $\mu\text{m}$ , higher than that of loess from sections at Lingtai (LT; 20–22  $\mu\text{m}$ ), Beiguoyuan (BGY; 28–38  $\mu\text{m}$ ), and Luochuan (LC; 18–22  $\mu\text{m}$ ) on the central CLP (Sun *et al.*, 2006; Liu *et al.*, 2020). Our loess samples also feature a minor peak at  $\sim 450$   $\mu\text{m}$ , indicating the presence of coarse sand. Loess is transported as

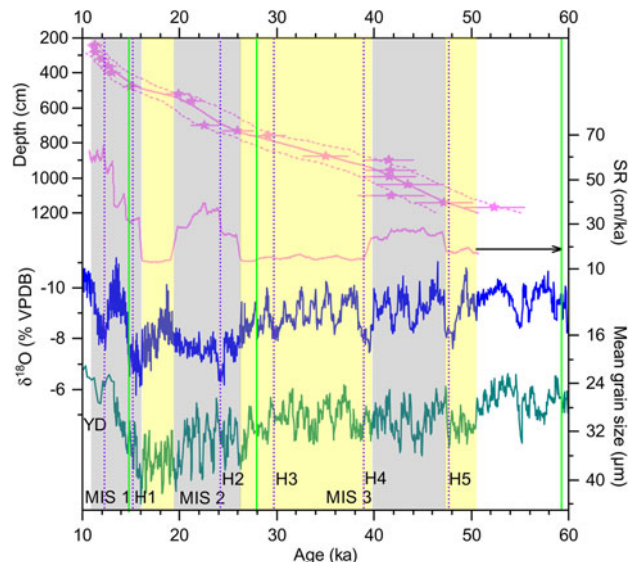


**Figure 8.** Comparison of quartz optically stimulated luminescence (OSL) ages and calculated sedimentation rate (SR; magenta) with composite Asian monsoon  $\delta^{18}\text{O}$  record of speleothems (blue; Cheng *et al.*, 2016) and Gulang loess mean grain size (green; Sun *et al.*, 2012). The Bacon model results are shown as solid (weighted mean age) and dashed (2-sigma uncertainty envelope) lines. The shaded regions represent the episodes of high (gray) and low (yellow) SR (cm/ka). The violet dashed lines represent the Younger Dryas event (YD) and Heinrich events 1–5 (H1–H5; Bond *et al.*, 1993). The green solid lines represent the boundaries of Marine Isotope Stages (MIS), defined after Martinson *et al.* (1987) and Sanchez Goñi and Harrison (2010).



aeolian sediment from north to south and west to east (Liu, 1985), with the mean grain size showing a decreasing trend with transportation distance (Yang and Ding, 2017). However, our results reveal that Malan loess from the SMG on the southern CLP is coarser than that found on the central CLP. One possible explanation is that core SMX19 was drilled ~450 m from the banks of the YR. Consequently, we deduce that part of the loess must have originated from the local YR floodplain. This observation aligns with findings from the loess–palaeosol sequence in Mangshan, located ~250 km downstream of the SMG, wherein the YR floodplain was identified as a significant source of dust (Jiang et al., 2007; Shang et al., 2018).

### Loess SR change in the SMG region

The OSL dates indicate that the initiation of loess deposition in our core occurred around ~52.4 ka (Fig. 8, Table 1), significantly later than the formation age of T2, which is approximately ~129 ka (Hu et al., 2017; Wang et al., 2022). Moreover, the dating results reveal a consistent pattern of loess deposition in our core within the stratigraphic sequences spanning from 52.4 to 11.3 ka. An exception is noted in the case of one sample, SMX19-16, representing an age reversal. The OSL age of  $43.5 \pm 3.2$  ka for this particular sample (depth 10.4 m) aligns with the date of  $41.8 \pm 3.4$  ka for the lower sample within OSL dating errors (SMX19-17, depth 11.0 m). This alignment contributes to our confidence in the reliability of our OSL dates. Despite the limited sampling resolution, two age gaps are evident between 40–30 and 20–13 ka, respectively (Supplementary Fig. S3). Such characteristics could potentially be interpreted as indicative of either a low SR or a deposition hiatus. As depicted in Figure 1, the WN and SMG loess sites are both situated in the Weihe Basin, with a distance of ~150 km. Supplementary Figure S3 illustrates that the variations in OSL ages versus depth are roughly similar between the two sites, suggesting that they were influenced by similar forces. The OSL dates indicate loess deposition between 10 and 54 ka in WN, with no apparent hiatus on a millennial scale, implying that the age gaps in SMG would be interpreted as indicative of a low SR. This hypothesis gains further support from SR values, indicating that the SR in SMG was higher than in WN throughout the entire deposition time period, likely due to its proximity to the YR floodplain.

Thus, we further investigated the SR variations in the SMG. As depicted in Figure 8, the SR changes exhibit six episodes, consisting of three high and three low episodes. The mean SRs for these episodes were approximately ~18.1, ~26.0, ~14.9, ~31.9, ~13.7, and ~49.9 cm/ka for the periods between 50.7–47.4, 47.4–39.7, 39.7–26.2, 26.2–19.8, 19.8–16.1, and 16.1–10.7 ka, respectively. The mean values of the high SR episodes (i.e., ~26.0, 31.9, and 49.9 cm/ka) were about twice as high as those for the low SR episodes (i.e., ~18.1, ~14.9, and ~13.7 cm/ka), indicating clear changes in the SRs within the core.

Loess deposition can be influenced by three main factors: dust emission from the source area, atmospheric transportation, and land surface capture (e.g., Kohfeld and Harrison, 2001; Maher et al., 2010; Kang et al., 2015; Újvári et al., 2016). Normally, dust emissions from the source area and the strength of the East Asian winter monsoon (EAWM) would be intensified during glacial periods (Marine Isotope Stage [MIS] 2) compared with interglacial periods (MIS 1). This intensification would result in enhanced loess accumulation (An et al., 1991a; Porter, 2001; Kohfeld and Harrison, 2003). However, the data

presented suggest that high SR episodes occurred during the middle of MIS 3, MIS 2, and early MIS 1 (Fig. 8). The high SR episodes at 16.1–10.7 and 26.2–19.8 ka roughly align with the time periods of Heinrich event 1 (H1) to the Younger Dryas Event (YD) and Heinrich event 2 (H2), respectively. The EAWM intensified during these rapid cooling events (Sun et al., 2012), suggesting that loess aggradation in the SMG would have likely occurred during colder and drier climatic periods. However, the high SR episode between 47.4 and 39.7 ka corresponds to the middle MIS 3 chronozone, when the climate was warm and wet (Wang et al., 2001; Cheng et al., 2016). The shrinking floodplain of the YR and denser and more extensive vegetation cover during such warm and wet climatic conditions both would have hindered dust emissions in the SMG region. Previously, the occurrence of a high SR episode during MIS 3 was attributed to heightened dust deposition efficiency linked with raised precipitation and vegetation, as observed in loess sections from Luochuan and Weinan (Lu et al., 2007; Kang et al., 2013). A comparable mechanism may govern the high SR episode during the middle MIS 3 chronozone in the SMG. However, this explanation fails to elucidate the low SR episode during the late MIS 3 chronozone, suggesting that variations in SR may be influenced by complex driving forces

### Loess sections with high-resolution OSL dating across the CLP

The majority of the OSL ages demonstrate loess deposition shows no apparent hiatus on a millennial scale, with two exceptions at ZBT and JB, indicating the presence of large hiatuses (>20 ka) in only a few loess sections (Fig. 9a–g). Most OSL ages were determined using quartz, while only two sections (ZBT and JB) were dated using both quartz and K-feldspar. For the section at JB, the quartz and K-feldspar ages of the same sample were roughly consistent within a 20% error (Fig. 9b). However, the situation was more complex for samples from the section at ZBT. The OSL ages of <~20 ka for quartz and K-feldspar were consistent within a 10% error, but quartz yielded much younger ages (>24 ka) than K-feldspar, which gave OSL ages of >26 ka. Wu et al. (2019) argued that the saturation dose of quartz in the ZBT section was ~150 Gy. This could imply that the quartz OSL age might have been underestimated, and the K-feldspar-derived age is closer to the actual burial time of the sediment (Wu et al., 2019). Conversely, Li et al. (2015) reported that the saturation dose ( $2D_0$ ) for quartz across China is ~230 Gy. This suggests that the quartz “saturation” effect was different across the CLP, which may be related to different source areas, and a cross-check between quartz OSL dating and K-feldspar or polymineral pIRIR dating should be routinely conducted for samples with greater  $D_e$  values (>150 Gy).

### Uniformity of SR changes across the CLP

The SR curves for various sections exhibit several high and low SR episodes within the past 60 ka (Fig. 10). To facilitate a comparison of changes in SRs among different sections, the mean values of these episodes were calculated, as illustrated in Figure 11.

#### MIS 3 (59.4–27.8 ka)

Ten sections (GL, JY, XF, LT, XY, LC, YX SGZ, WN, and SMG) across the CLP exhibit high SR episodes during MIS 3, while two sections (ZBT and JB) on the margins of the Mu Us Desert

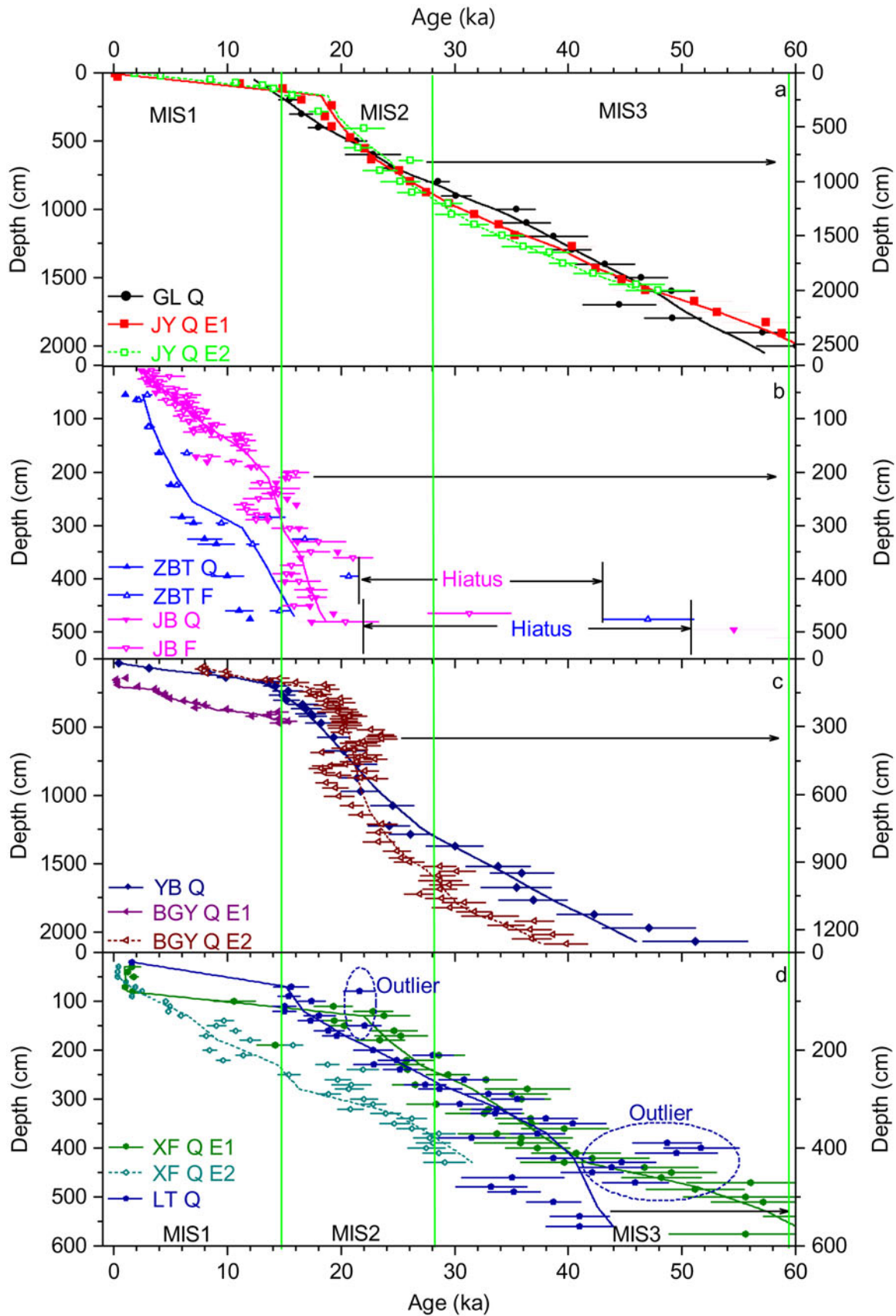


**Figure 9.** (a–g) Plots of optically stimulated luminescence (OSL) ages vs. depth, for different sites; full names and references are listed in Table 2. The solid and dashed lines represent the Bacon age–depth model results; the errors of the model results were not added for ease of viewing. The green solid lines represent the boundaries of Marine Isotope Stages (MIS), defined after Martinson *et al.* (1987) and Sanchez Goñi and Harrison (2010). See Table 2 for site abbreviations.

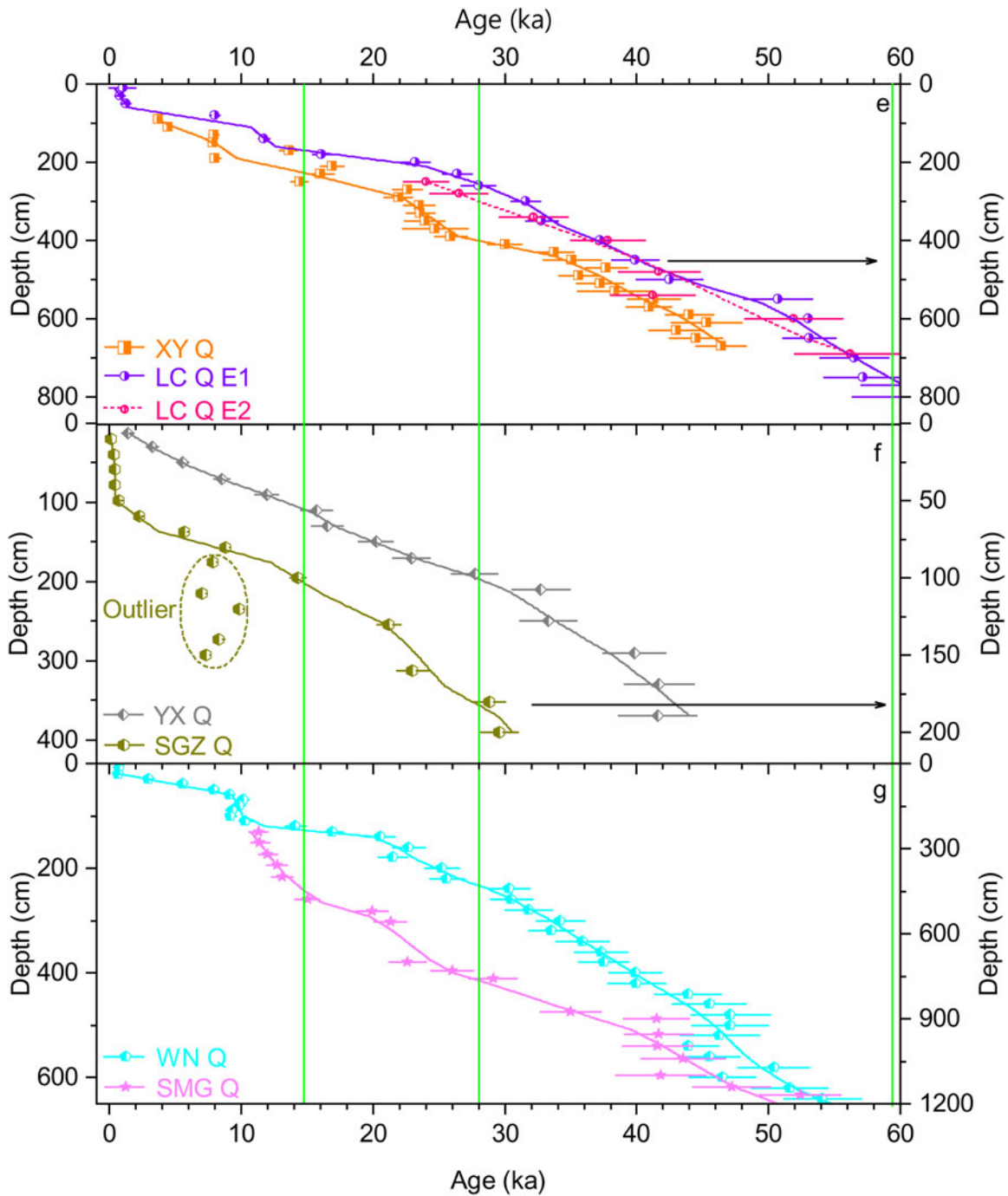
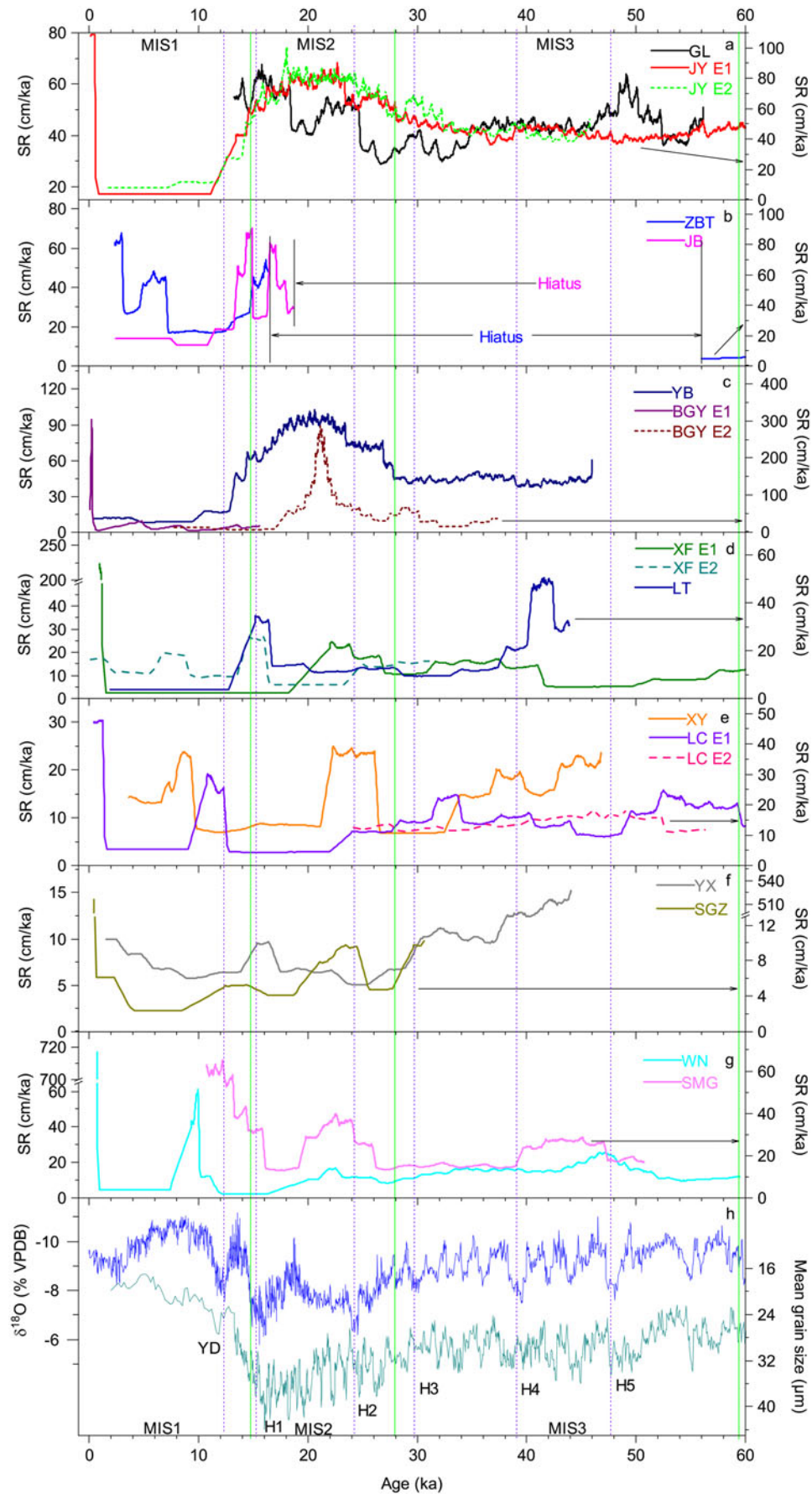


Figure 9. Continued.

indicate depositional hiatuses during MIS 2–MIS 3 (Figs. 9b, 10, and 11). Stevens et al. (2018) suggested that the hiatus during MIS 2–MIS 3 observed in the JB section could be linked to increased dune mobility leading to the erosion of the underlying strata, a hypothesis further supported by the analysis of the ZBT section (Wu et al., 2019). Previous research has also indicated erosional hiatuses in loess deposits in the southern Tengger Desert during 40–25 ka (Qiang et al., 2021; Peng et al., 2022). The mechanism behind the scarcity of aeolian deposits in the Mu Us Desert and Tengger Desert margins during MIS 3 remains unclear (Stevens

et al., 2018; Peng et al., 2022). However, summer monsoon intensity was also enhanced during MIS 3 (Cheng et al., 2016). The increased precipitation associated with this intensification of the East Asian summer monsoon (EASM) would have elevated dust deposition efficiency (Kang et al., 2013), and a denser and more widespread vegetation cover would have improved the dust-capture ability of the land surface (Lu et al., 2007). High SR episodes during MIS 3 across the CLP might, therefore, be explained by enhanced dust deposition efficiency related to increases in precipitation and vegetation.



**Figure 10.** (a–g) The calculated sedimentation rates (SR) based on the Bacon age–depth model for different sites; full names and references are listed in Table 2. (h) Composite Asian monsoon  $\delta^{18}\text{O}$  record of speleothems (blue; Cheng et al., 2016) and Gulang loess mean grain size (green; Sun et al., 2012). The violet dashed lines represent the Younger Dryas event (YD) and Heinrich events 1–5 (H1–H5; Bond et al., 1993). The green solid lines represent the boundaries of Marine Isotope Stages (MIS), defined after Martinson et al. (1987) and Sanchez Goñi and Harrison (2010). See Table 2 for site abbreviations.

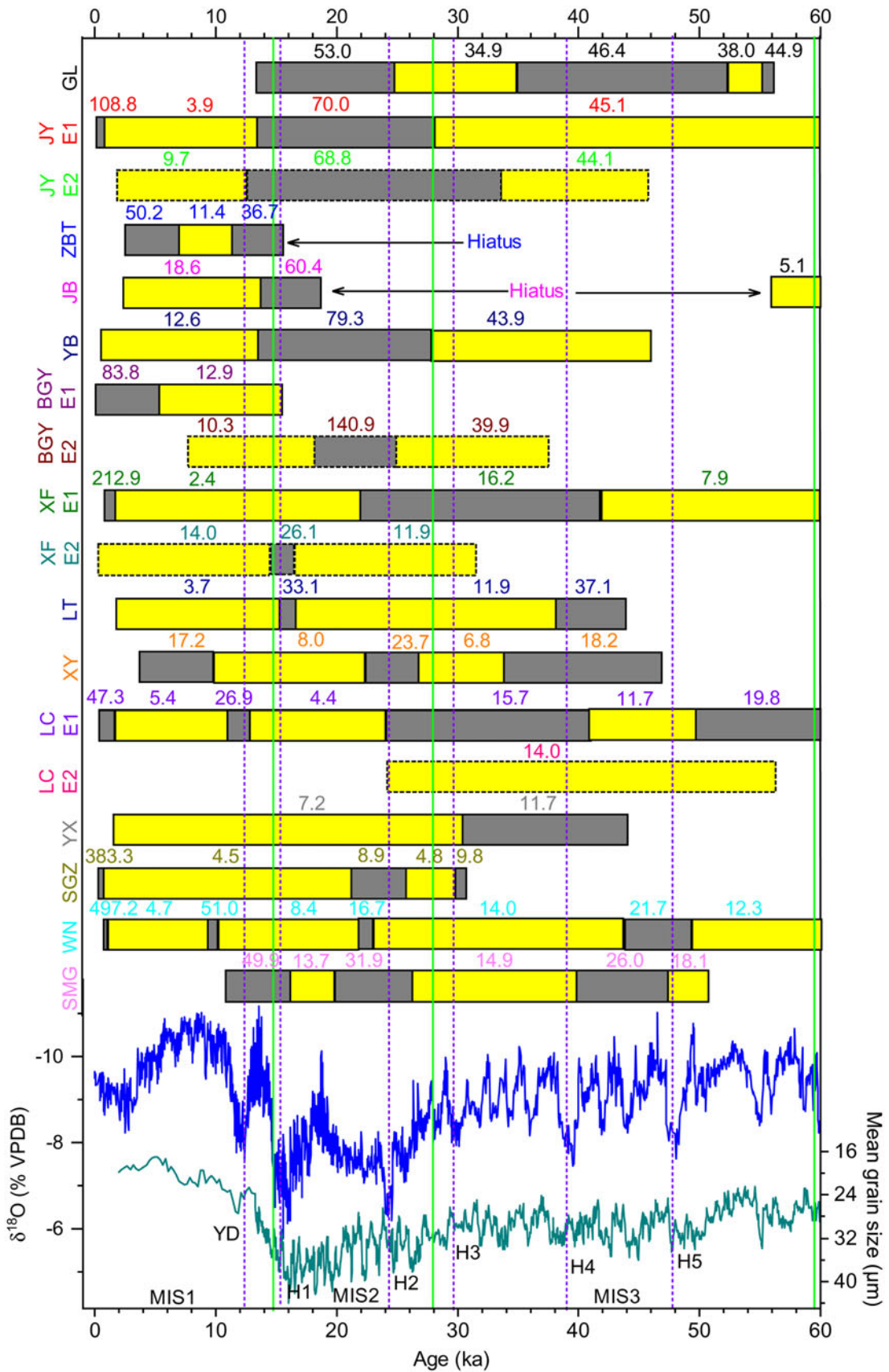


**Figure 11.** Comparison of high (gray bar) and low (yellow bar) sedimentation rate (SR; cm/ka) episodes with composite Asian monsoon  $\delta^{18}O$  record of speleothems (blue; Cheng et al., 2016) and Gulang loess mean grain size (green; Sun et al., 2012). The violet dashed lines represent the Younger Dryas event (YD) and Heinrich events 1–5 (H1–H5; Bond et al., 1993). The green solid lines represent the boundaries of Marine Isotope Stages (MIS), defined after Martinson et al. (1987) and Sanchez Goñi and Harrison (2010). See Table 2 for site abbreviations.

### MIS 2 (27.8–14.7 ka)

All the sites across the CLP exhibited high SR episodes during MIS 2, except for YX. High SR episodes in four loess sections at three sites (GL, JY, and YB) persisted throughout the entire MIS 2 (Fig. 10a and c). The continuation of high SR episodes during MIS 2 in the other 14 sections from 11 sites (ZBT, JB, BGY, XF, LT, XY, LC, YX, SGZ, WN, and SMG) lasted only for a few thousand years (Fig. 11, Table 2). The temporal distribution of these high SR episodes appears highly scattered. High SR episodes during the LGM (~23–19 ka) occurred at two sites (BGY and WN) (Sanchez Goñi and Harrison, 2010); during H2, at four sites (BGY, XY, SGZ, and SMG); and during H1, at five sites (ZBT, JB, XF, LT, and SMG).

Three sites (GL, YB, and JY) are situated along the western margins of the CLP, with the Tengger Desert to their north and the Qilian and eastern Kunlun Mountains to their southwest (Fig. 1). Dust transported from the Tengger Desert would likely have been blocked by the Qilian and eastern Kunlun Mountains. Sedimentary deposition in the Tengger Desert exhibited a hiatus during the 40–25 ka period, followed by the deposition of large quantities of sandy loess and aeolian sand during 22–10 ka (Qiang *et al.*, 2021; Peng *et al.*, 2022), suggesting enhanced dust emissions from the source regions during this time. Kang *et al.* (2015) and Xu *et al.* (2018) argued that rapid dust accumulation during the LGM was linked to a greatly intensified EAWM. Therefore, high SR episodes during MIS 2 across the CLP could be explained by the combined action of dust emission from the source areas and an intensified EAWM.

### MIS 1 (14.7–0 ka)

As depicted in Figures 10 and 11, most sites experienced low SR episodes during MIS 1. Only three sites (ZBT, LC, and SMG) showed high SR episodes during the YD, with low SR episodes occurring at the same period in the other 11 sites. The SRs for nine sites (JY, JB, YB, XF, LT, LC, YX, SGZ, and WN) exhibited their lowest values during the Early to Late Holocene. Loess mean grain sizes in sections from the GL and JY sites decreased after 15 ka, indicating a weakening EAWM wind strength (Sun *et al.*, 2012). Conversely, pollen data indicate a significant increase in vegetation cover during this period, along with the development of paleosols (S0) (Zhou *et al.*, 2014; Yang *et al.*, 2015). The low SR episodes during MIS 1 could therefore be related to reduced atmospheric transportation and pedogenesis.

It should be noted that five sites (JY, XF, LC, SGZ, and WN) experienced unusually high SR episodes (1.6–0.1 ka) during the Late Holocene (Table 2). The mean values for these high SR episodes ranged from 108.8 cm/ka (JY, 0.8–0.1 ka) to 497.2 cm/ka (WN, 0.74–0.69 ka), representing a surge of 9 to 105 times higher than the mean values of previous low SR episodes (Fig. 11). Chen *et al.* (2021) argued that the largest fluctuation in dust storms recorded during the past 2 ka in the Gonghai Lake area (northwestern CLP) could be linked to human activity. Zhao *et al.* (2022) calculated changes in SR across the CLP during the Holocene and identified several high SR episodes during the past 2 ka that might be associated with significant increases in the human population in dust source areas.

### Spatiotemporal heterogeneity of SR changes across the CLP

Moreover, in addition to the common characteristics observed in changes in SRs, the SR curves for loess sections across the CLP also exhibit some spatiotemporal heterogeneity during the last

60 ka (Figs. 10 and 11). Apart from the abnormally high SR observed during the Late Holocene (<2 ka), eight sections from six sites located on the western, northern, and northeastern CLP (ZBT, JB, BGY, JY, YB, and GL) yielded the highest mean SR values. Seven sections from five sites (XF, LT, XY, YX, and LC) on the central CLP yielded the lowest mean SR values. This aligns with the transportation pathway of loess in China (Liu, 1985): sites closer to the source area would be expected to have higher SRs. However, the SR values in two sections (WN and SMG) on the southern CLP were higher than at sites on the central CLP. This is consistent with the grain-size distribution results discussed earlier. We would suggest that the influence of the local aeolian dust source of the YR floodplain, combined with the blocking effect of the Qinling Mountain range, might be the principal reason for these high SRs at the WN and SMG sites.

The SRs of the loess sections also experienced some temporal heterogeneity over the last 60 ka (Figs. 10 and 11), potentially caused by local geologic/geomorphological factors. The high SR episodes during MIS 3 for different loess sections were temporally heterogeneous (Table 2); most of these were inconsistent with the Heinrich events, suggesting that these high SRs were controlled by other drivers, rather than climate change (H3 to H5; Figs. 10 and 11). We also observed periods with low SRs lasting >4 ka during MIS 2 at six sites (XF, LT, XY, LC, YX, and WN). The mean SRs of these episodes were lower than, or roughly consistent with, those of the low SR episodes observed during MIS 3. As discussed earlier, source dust emissions during MIS 2 were higher than during MIS 3. This evidence would suggest that, in addition to local drivers (*i.e.*, dust emission, precipitation, and vegetation), changes in the local depositional environment also might have played a key role in driving SR change.

## CONCLUSION

A 9.8 m Malan loess core was extracted from the SMG region, situated on the southern CLP, and its age–depth model was established through OSL dating. The chronological analysis indicated that the loess deposition occurred between 52.4 and 11.3 ka. The observed variations in SRs suggest influences beyond paleoclimate changes. In an extensive review encompassing 613 OSL ages derived from 18 sections at 14 sites across the CLP, it was found that loess deposition shows no apparent hiatus on a millennial scale over the past 60 ka at most sites, with exceptions noted at two sites along the margins of the Mu Us Desert. The SR patterns exhibited some similarities across different sites. During MIS 3, high SR episodes across the CLP were attributed to increased dust source emissions and enhanced dust deposition efficiency, while those in MIS 2 were associated with an intensified EAWM. Low SR episodes during MIS 1 were linked to reduced atmospheric transport and pedogenesis. Human activities during the Late Holocene induced abnormally high SR episodes (ranging from ~108.8 to 497.2 cm/ka), exceeding those observed during the Early to Mid-Holocene (ranging from ~3.9 to 12.6 cm/ka) by at least ninefold. Spatially heterogeneous SR variations across the CLP might be influenced by local depositional environments.

**Acknowledgments.** We should like to thank H.L. Yang for help with laboratory dating. We should like to thank Y.B. Sun and X.X. Liu for help with providing loess grain-size data.

**Funding.** This work was supported by the National Non-Profit Fundamental Research Grant of China (grant no. IGCEA 2008) and the National Natural

Science Foundation of China (grant nos. 41271018, 41230523, 40971017, and 41471006).

**Competing Interests.** The authors declare no competing interests.

## REFERENCES

- An, Z., Kukla, G., Porter, S.C., Xiao, J., 1991a. Late Quaternary dust flow on the Chinese Loess Plateau. *Catena* **18**, 125–132.
- An, Z., Kukla, G.J., Porter, S.C., Xiao, J., 1991b. Magnetic susceptibility evidence of monsoon variation on the Loess Plateau of Central China during the last 130,000 years. *Quaternary Research* **36**, 29–36.
- An, Z., Wang, J., Li, H., 1977. Paleomagnetic research of the Luochuan loess section. *Geochimica* **4**, 239–249.
- Blaauw, M., Christen, J.A., 2011. Flexible paleoclimate age-depth models using an autoregressive gamma process. *Bayesian Analysis* **6**, 457–474.
- Bond, G., Broecker, W., Johnsen, S., McManus, J., Labeyrie, L., Jouzel, J., Bonani, G., 1993. Correlations between climate records from North Atlantic sediments and Greenland ice. *Nature* **365**, 143–147.
- Chen, S., Liu, J., Wang, X., Zhao, S., Chen, J., Qiang, M., Liu, B., Xu, Q., Xia, D., Chen, F., 2021. Holocene dust storm variations over northern China: transition from a natural forcing to an anthropogenic forcing. *Science Bulletin* **66**, 2516–2527.
- Cheng, H., Edwards, L., Sinha, A., Spötl, C., Yi, L., Chen, S., Kelly, M., et al. 2016. The Asian monsoon over the past 640,000 years and ice age terminations. *Nature* **534**, 640–646.
- Constantin, D., Mason, J.A., Veres, D., Hambach, U., Panaiotu, C., Zeeden, C., Zhou, L., et al. 2021. OSL-dating of the Pleistocene-Holocene climatic transition in loess from China, Europe and North America, and evidence for accretionary pedogenesis. *Earth-Science Reviews* **221**, 103769.
- Ding, Z.L., Derbyshire, E., Yang, S.L., Yu, Z.W., Xiong, S.F., Liu, T.S., 2002. Stacked 2.6–Ma grain size record from the Chinese loess based on five sections and correlation with the deep-sea  $\delta^{18}\text{O}$  record. *Paleoceanography* **17**, 1033.
- Dong, Y., Wu, N., Li, F., Huang, L., Wen, W., 2015. Time-transgressive nature of the magnetic susceptibility record across the Chinese Loess Plateau at the Pleistocene/Holocene transition. *PLoS ONE* **10**, e0133541.
- Duller, G.A.T., 2003. Distinguishing quartz and feldspar in single grain luminescence measurements. *Radiation Measurements* **37**, 161–165.
- Fu, X., Li, B., Li, S.H., 2012. Testing a multi-step post-IR IRSL dating method using polymineral fine grains from Chinese loess. *Quaternary Geochronology* **10**, 8–15.
- Hu, Z., Pan, B., Bridgland, D., Vandenberghe, J., Guo, L., Fan, Y., Westaway, R., 2017. The linking of the upper-middle and lower reaches of the Yellow River as a result of fluvial entrenchment. *Quaternary Science Reviews* **166**, 324–338.
- Jiang, F., Fu, J., Wang, S., Sun, D., Zhao, Z., 2007. Formation of the Yellow River, inferred from loess–paleosol sequence in Mangshan and lacustrine sediments in Sanmen Gorge, China. *Quaternary International* **175**, 62–70.
- Kang, S., Roberts, H.M., Wang, X., An, Z., Wang, M., 2015. Mass accumulation rate changes in Chinese loess during MIS 2, and asynchrony with records from Greenland ice cores and North Pacific Ocean sediments during the Last Glacial Maximum. *Aeolian Research* **19**, 251–258.
- Kang, S., Wang, X., Lu, Y., 2013. Quartz OSL chronology and dust accumulation rate changes since the Last Glacial at Weinan on the southeastern Chinese Loess Plateau. *Boreas* **42**, 815–829.
- Kang, S.G., Lu, Y.C., Wang, X.L., 2011. Closely-spaced recuperated OSL dating of the last interglacial paleosol in the southeastern margin of Chinese Loess Plateau. *Quaternary Geochronology* **6**, 480–490.
- Kohfeld, K.E., Harrison, S.P., 2001. DIRTMAP: the geological record of dust. *Earth-Science Reviews* **54**, 81–114.
- Kohfeld, K.E., Harrison, S.P., 2003. Glacial-interglacial changes in dust deposition on the Chinese Loess Plateau. *Quaternary Science Reviews* **22**, 1859–1878.
- Konert, M., Vandenberghe, J.E.F., 1997. Comparison of laser grain size analysis with pipette and sieve analysis: a solution for the underestimation of the clay fraction. *Sedimentology* **44**, 523–535.
- Kukla, G., Heller, F., Liu, X.M., Xu, T.C., Liu, T.S., An, Z.S., 1988. Pleistocene climates in China dated by magnetic susceptibility. *Geology* **16**, 811.
- Lai, Z., 2010. Chronology and the upper dating limit for loess samples from Luochuan section in the Chinese Loess Plateau using quartz OSL SAR protocol. *Journal of Asian Earth Sciences* **37**, 176–185.
- Lai, Z.P., Wintle, A.G., 2006. Locating the boundary between the Pleistocene and the Holocene in Chinese loess using luminescence. *The Holocene* **16**, 893–899.
- Li, B., Li, S.H., 2011. Luminescence dating of K-feldspar from sediments: a protocol without anomalous fading correction. *Quaternary Geochronology* **6**, 468–479.
- Li, B., Roberts, R.G., Jacobs, Z., Li, S.H., 2015. Potential of establishing a “global standardized growth curve” (gSGC) for optical dating of quartz from sediments. *Quaternary Geochronology* **27**, 94–104.
- Li, G., Chen, F., Xia, D., Yang, H., Zhang, X., Madsen, D., Oldknow, C., Wei, H., Rao, Z., Qiang, M., 2018. A Tianshan Mountains loess-paleosol sequence indicates anti-phase climatic variations in arid central Asia and in East Asia. *Earth and Planetary Science Letters* **494**, 153–163.
- Li, G.Q., Rao, Z.G., Duan, Y.W., Xia, D.S., Wang, L.B., Madsen, D.B., Jia, J., Wei, H.T., Qiang, M.R., Chen, F.H., 2016. Paleoenvironmental changes recorded in a luminescence dated loess/paleosol sequence from the Tianshan Mountains, arid central Asia, since the penultimate Glaciation. *Earth and Planetary Science Letters* **448**, 1–12.
- Li, H., An, Z.S., Wang, J., 1974. Preliminary palaeomagnetic results of a loess profile at Wucheng. *Geochimica* **2**, 93–103.
- Li, S.H., Wintle, A.G., 1992. A global view of the stability of luminescence signals from loess. *Quaternary Science Reviews* **11**, 133–137.
- Li, X., Ao, H., Dekkers, M.J., Roberts, A.P., Zhang, P., Lin, S., Huang, W., Hou, Y., Zhang, W., An, Z., 2017. Early Pleistocene occurrence of Acheulian technology in North China. *Quaternary Science Reviews* **156**, 12–22.
- Liu, T.S., 1985. *Loess and the Environment*. [In Chinese.] China Ocean Press, Beijing.
- Liu, Y., Liu, X., Ma, L., Kang, S., Qiang, X., Guo, F., Sun, Y., 2020. Temporal–spatial variations in aeolian flux on the Chinese Loess Plateau during the last 150 ka. *Geological Magazine* **157**, 757–767.
- Lu, H., Liu, X., Zhang, F., An, Z., Dodson, J., 1999. Astronomical calibration of loess–paleosol deposits at Luochuan, central Chinese Loess Plateau. *Palaeogeography, Palaeoclimatology, Palaeoecology* **154**, 237–246.
- Lu, Y.C., Wang, X.L., Wintle, A.G., 2007. A new OSL chronology for dust accumulation in the last 130,000 yr for the Chinese Loess Plateau. *Quaternary Research* **67**, 152–160.
- Maher, B.A., 2016. Palaeoclimatic records of the loess/paleosol sequences of the Chinese Loess Plateau. *Quaternary Science Reviews* **154**, 23–84.
- Maher, B.A., Prospero, J.M., Mckie, D., Gaiero, D., Hesse, P.P., Balkanski, Y., 2010. Global connections between aeolian dust, climate and ocean biogeochemistry at the present day and at the last glacial maximum. *Earth-Science Reviews* **99**, 61–97.
- Martinson, D.G., Pisias, N.G., Hays, J.D., Imbrie, J., Moore, T.C., Shackleton, N.J., 1987. Age dating and orbital theory of the Ice Ages: development of a high-resolution 0 to 300,000-year chronostratigraphy. *Quaternary Research* **27**, 1–29.
- Murray, A.S., Wintle, A.G., 2000. Luminescence dating of quartz using an improved single-aliquot regenerative-dose protocol. *Radiation Measurements* **32**, 57–73.
- Murray, A.S., Wintle, A.G., 2003. The single aliquot regenerative dose protocol: potential for improvements in reliability. *Radiation Measurements* **37**, 377–381.
- Peng, J., Wang, X., Yin, G., Adamiec, G., Du, J., Zhao, H., Kang, S., Hu, G., Zheng, Y., 2022. Accumulation of aeolian sediments around the Tengger Desert during the late Quaternary and its implications on interpreting chronostratigraphic records from drylands in north China. *Quaternary Science Reviews* **275**, 107288.
- Perić Z., Adophi E.L., Buylaert J.P., Stevens T., Újvári G., Marković S.B., Hambach U., et al., 2019. Quartz OSL dating of late Quaternary Chinese and Serbian loess: a cross Eurasian comparison of dust mass accumulation rates. *Quaternary International* **502**, 30–44.
- Porter, S.C., 2001. Chinese loess record of monsoon climate during the last glacial-interglacial cycle. *Earth-Science Reviews* **54**, 115–128.

- Porter, S.C., An, Z., 1995. Correlation between climate events in the North Atlantic and China, during the last glaciation. *Nature* **375**, 305–308.
- Qiang, M., Stevens, T., Li, G., Hu, L., Wang, X., Lang, W., Chen, J., 2021. Late Quaternary dust, loess and desert dynamics in upwind areas of the Chinese Loess Plateau. *Frontiers in Earth Science* **9**, 254.
- Rao, Z., Chen, F., Cheng, H., Liu, W., Wang, G.A., Lai, Z., Bloemendal, J., 2013. High-resolution summer precipitation variations in the western Chinese Loess Plateau during the last glacial. *Scientific Reports* **3**, 1–6.
- Sanchez Goñi, M.F., Harrison, S.P., 2010. Millennial-scale climate variability and vegetation changes during the Last Glacial: concepts and terminology. *Quaternary Science Reviews* **29**, 2823–2827.
- Shang, Y., Prins, M.A., Beets, C.J., Kaakinen, A., Lahaye, Y., Dijkstra, N., Rits, D.S., Wang, B., Zheng, H.B., van Balen, R.T., 2018. Aeolian dust supply from the Yellow River floodplain to the Pleistocene loess deposits of the Mangshan Plateau, central China: evidence from zircon U-Pb age spectra. *Quaternary Science Reviews* **182**, 131–143.
- Shangguan, R.G., 2021. Excavation report of trench tomb of Western Han Dynasty at Houchuan in Sanmenxia, Henan Province. [In Chinese.] *Journal of National Museum of China* **3**, 68–86.
- Stevens, T., Adamiec, G., Bird, A. F., Lu, H., 2013. An abrupt shift in dust source on the Chinese Loess Plateau revealed through high sampling resolution OSL dating. *Quaternary Science Reviews* **82**, 121–132.
- Stevens, T., Armitage, S.J., Lu, H., Thomas, D.S., 2006. Sedimentation and diagenesis of Chinese loess: implications for the preservation of continuous, high-resolution climate records. *Geology* **34**, 849–852.
- Stevens, T., Buylaert, J.P., Lu, H., Thiel, C., Murray, A., Frechen, M., Yi, S., Zeng, L., 2016. Mass accumulation rate and monsoon records from Xifeng, Chinese Loess Plateau, based on a luminescence age model. *Journal of Quaternary Science* **31**, 391–405.
- Stevens, T., Buylaert, J.P., Thiel, C., Újvári, G., Yi, S., Murray, A.S., Frechen, M., Lu, H., 2018. Ice-volume-forced erosion of the Chinese Loess Plateau global Quaternary stratotype site. *Nature Communications* **9**, 1–12.
- Stevens, T., Lu, H., Thomas, D.S.G., Armitage, S.J., 2008. Optical dating of abrupt shifts in the Late Pleistocene East Asian monsoon. *Geology* **36**, 415–418.
- Stevens, T., Thomas, D.S., Armitage, S.J., Lunn, H.R., Lu, H., 2007. Reinterpreting climate proxy records from late Quaternary Chinese loess: a detailed OSL investigation. *Earth-Science Reviews* **80**, 111–136.
- Sun, D.H., Bloemendal, J., Rea, D.K., Vandenberghe, J., Jiang, F.C., An, Z.S., Su, R.X., 2002. Grain-size distribution function of polymodal sediments in hydraulic and aeolian environments, and numerical partitioning of the sedimentary components. *Sedimentary Geology* **152**, 263–277.
- Sun, J., 2002. Provenance of loess material and formation of loess deposits on the Chinese Loess Plateau. *Earth and Planetary Science Letters* **203**, 845–859.
- Sun, Y., Clemens, S.C., Morrill, C., Lin, X., Wang, X., An, Z., 2012. Influence of Atlantic meridional overturning circulation on the East Asian winter monsoon. *Nature Geoscience* **5**, 46–49.
- Sun, Y., Lu, H., An, Z., 2006. Grain size of loess, paleosol and Red Clay deposits on the Chinese Loess Plateau: significance for understanding pedogenic alteration and palaeomonsoon evolution. *Palaeogeography, Palaeoclimatology, Palaeoecology* **241**, 129–138.
- Sun, Y., Wang, X., Liu, Q., Clemens, S.C., 2010. Impacts of post-depositional processes on rapid monsoon signals recorded by the last glacial loess deposits of northern China. *Earth and Planetary Science Letters* **289**, 171–179.
- Tsakalos, E., Christodoulakis, J., Charalambous, L., 2015. The Dose Rate Calculator (DRc) for luminescence and ESR dating—a java application for dose rate and age determination. *Archaeometry* **58**, 347–352.
- Újvári, G., Kok, J.F., Varga, G., Kovács, J., 2016. The physics of wind-blown loess: implications for grain size proxy interpretations in Quaternary paleoclimate studies. *Earth-Science Reviews* **154**, 247–278.
- Wang, S., Fu, B., Piao, S., Lü, Y., Ciais, P., Feng, X., Wang, Y., 2016. Reduced sediment transport in the Yellow River due to anthropogenic changes. *Nature Geoscience* **9**, 38–41.
- Wang, X., Hu, G., Saito, Y., Ni, G., Hu, H., Yu, Z., Chen, J., et al. 2022. Did the modern Yellow River form at the mid-Pleistocene transition? *Science Bulletin* **67**, 1603–1610.
- Wang, Y.J., Cheng, H., Edwards, R.L., An, Z.S., Wu, J.Y., Shen, C.C., Dorale, J.A., 2001. A high-resolution absolute-dated Late Pleistocene monsoon record from Hulu Cave, China. *Science* **294**, 2345–2348.
- Wintle, A.G., Murray, A.S., 2006. A review of quartz optically stimulated luminescence characteristics and their relevance in single aliquot regeneration dating protocols. *Radiation Measurements* **41**, 369–391.
- Wu, J., Lu, H., Yi, S., Xu, Z., Gu, Y., Liang, C., Cui, M., Sun, X., 2019. Establishing a high-resolution luminescence chronology for the Zhenbeitai sand-loess section at Yulin, north-central China. *Quaternary Geochronology* **49**, 78–84.
- Xiong, J., Li, Y., Zheng, W., Zhang, P., Lei, J., Zhong, Y., Hu, X., et al. 2018. Climatically driven formation of the Tangxian planation surface in North China: an example from northwestern Zhongtiao Shan of the Shanxi Graben System. *Lithosphere* **10**, 530–544.
- Xiong, J., Li, Y., Zhong, Y., Si, S., Lei, J., Xin, W., Hu, X., Yao, Y., 2017. Paleomagnetic age of the Tangxian planation surface, northwestern Zhongtiao Shan of the Shanxi Graben System, North China. *Geomorphology* **283**, 17–31.
- Xiong, L.Y., Tang, G.A., Li, F.Y., Yuan, B.Y., Lu, Z.C., 2014. Modeling the evolution of loess-covered landforms in the Loess Plateau of China using a DEM of underground bedrock surface. *Geomorphology* **209**, 18–26.
- Xu, Z., Stevens, T., Yi, S., Mason, J. A., Lu, H., 2018. Seesaw pattern in dust accumulation on the Chinese Loess Plateau forced by late glacial shifts in the East Asian monsoon. *Geology* **46**, 871–874.
- Yang, S., Ding, Z., 2017. Spatial changes in grain size of loess deposits in the Chinese Loess Plateau and implications for paleoenvironment. *Quaternary Sciences* **37**, 934–944.
- Yang, S., Ding, Z., Li, Y., Wang, X., Jiang, W., Huang, X., 2015. Warming-induced northwestward migration of the East Asian monsoon rain belt from the Last Glacial Maximum to the mid-Holocene. *Proceedings of the National Academy of Sciences USA* **112**, 13178–13183.
- Yi, S., Buylaert, J.P., Murray, A.S., Thiel, C., Zeng, L., Lu, H., 2015. High resolution OSL and post-IR IRSL dating of the last interglacial-glacial cycle at the Sanbahu loess site (northeastern China). *Quaternary Geochronology* **30**, 200–206.
- Zhang, J., Hao, Q., Li, S.H., 2022. An absolutely dated record of climate change over the last three glacial-interglacial cycles from Chinese loess deposits. *Geology* **50**, 1116–1120.
- Zhang, J.F., Zhou, L.P., 2007. Optimization of the “double SAR” procedure for polymineral fine grains. *Radiation Measurements* **42**, 1475–1482.
- Zhao, S., Xia, D., Lü, K., 2022. Holocene aeolian dust accumulation rates across the Chinese Loess Plateau. *Global and Planetary Change* **208**, 103720.
- Zhao, L., Lu, H., Wang, H., Meadows, M., Ma, C., Tang, L., Lei, F., Zhang, H., 2020. Vegetation dynamics in response to evolution of the Asian Monsoon in a warm world: pollen evidence from the Weihe Basin, Central China. *Global and Planetary Change* **193**, 103269.
- Zhou, X., Li, X., Dodson, J., Yang, S., Long, H., Zhao, K., Sun, N., Qing, Y., Liu, H., Zhao, C., 2014. Zonal vegetation change in the Chinese Loess Plateau since MIS 3. *Palaeogeography, Palaeoclimatology, Palaeoecology* **404**, 89–96.